ATLAS NOTE

ATLAS-CONF-2013-053

May 14, 2013

Search for direct third generation squark pair production in final states with missing transverse momentum and two b-jets in $\sqrt{s} = 8$ TeV pp collisions with the ATLAS detector.

The ATLAS Collaboration

Abstract

The result of a search for pair production of the supersymmetric partners of the Standard Model third generation quarks is reported. This search uses 20.1 fb^{-1} of pp collisions at $\sqrt{s} = 8$ TeV collected by the ATLAS experiment at the Large Hadron Collider. The lightest bottom and top squarks ($\tilde{b}_1$ and $\tilde{t}_1$ respectively) are searched for in a final state with large missing transverse momentum and two jets identified as originating from a b-quark. No excess of events above the expected level of Standard Model background is found. The results are used to set upper limits on the visible cross section of new phenomena. Exclusion limits at 95% confidence level on the masses of the third generation squarks are derived in phenomenological supersymmetric R-parity conserving models in which either the bottom or the top squark is the lightest squark. The $\tilde{b}_1$ is assumed to decay via $\tilde{b}_1 \rightarrow b\tilde{\chi}_1^0$ and the $\tilde{t}_1$ via $\tilde{t}_1 \rightarrow b\tilde{\chi}_1^{\pm}$, with undetectable products of the subsequent decay of the $\tilde{\chi}_1^{\pm}$ due to the small mass splitting between the $\tilde{\chi}_1^{\pm}$ and the $\tilde{\chi}_1^0$.

ATLAS-CONF-2013-053
16 May 2013

1 Introduction

Supersymmetry (SUSY) [1–9] provides an extension of the Standard Model (SM), which solves the hierarchy problem [10–13] by introducing supersymmetric partners of the known bosons and fermions. In the framework of the R-parity conserving minimal supersymmetric extension of the SM (MSSM) [14–18], SUSY particles are produced in pairs and the lightest supersymmetric particle (LSP) is stable, providing a possible candidate for dark matter. In a large variety of models, the LSP is the lightest neutralino ($\tilde{\chi}_1^0$). The coloured superpartners of quarks and gluons, the squarks ($\tilde{q}$) and the gluinos ($\tilde{g}$), if not too heavy, would be produced in strong interaction processes at the Large Hadron Collider (LHC) [19] and decay via cascades ending with the LSP. The undetected LSP would result in missing transverse momentum while the rest of the cascade would yield final states with multiple jets and possibly leptons.

A study of the expected SUSY particle spectrum derived from naturalness considerations [20, 21] suggests that the supersymmetric partners of the third generation SM quarks are the lightest coloured supersymmetric particles. This may lead to the lightest bottom squark (sbottom, $\tilde{b}_1$) and top squark (stop, $\tilde{t}_1$) mass eigenstates being significantly lighter than the other squarks and the gluinos. As a consequence, $\tilde{b}_1$ and $\tilde{t}_1$ could be produced with relatively large cross sections at the LHC.

Two assumptions on the SUSY mass spectrum are considered in this paper. In the first set of scenarios, the lightest sbottom is the only coloured sparticle contributing to the production processes and only the decay via $\tilde{b}_1 \rightarrow b\tilde{\chi}_1^0$ is considered. In the second set, the lightest stop is the only coloured sparticle allowed in the production processes and it decays exclusively via $\tilde{t}_1 \rightarrow b\tilde{\chi}_1^{\pm}$, where the lightest chargino ($\tilde{\chi}_1^{\pm}$) decays via a virtual W boson into the three-body final state $\tilde{\chi}_1^0 f \bar{f}'$. In the case of small values for $\Delta m \equiv m_{\tilde{\chi}_1^{\pm}} - m_{\tilde{\chi}_1^0}$, below 20 GeV, the fermions f and f' may have transverse momenta below the reconstruction thresholds applied in the analysis. In both cases events are characterised by the presence of two jets originating from the hadronisation of the b-quarks and large missing transverse momentum. Results of searches for direct sbottom and stop production have been previously reported by the ATLAS [22–27] and CMS [28–30] experiments at the LHC, the Tevatron [31, 32] and LEP [33] experiments.

2 The ATLAS detector and data samples

The ATLAS detector [34] consists of inner tracking devices surrounded by a superconducting solenoid, electromagnetic and hadronic calorimeters and a muon spectrometer with a toroidal magnetic field. The inner detector (ID), in combination with the 2 T field from the solenoid, provides precision tracking of charged particles in a pseudorapidity[1] range $|\eta| < 2.5$ and allows efficient identification of jets originating from b-hadron decays using impact parameter measurements to reconstruct secondary decay vertices. The ID consists of a silicon pixel detector, a silicon strip detector and a straw tube tracker that also provides transition radiation measurements for electron identification. The calorimeter system covers the pseudorapidity range $|\eta| < 4.9$. It is composed of sampling calorimeters with either liquid argon or scintillating tiles as the active medium. The muon spectrometer has separate trigger and high-precision tracking chambers, the latter provide muon identification and momentum measurement for $|\eta| < 2.7$.

The data sample used in this analysis was taken during the period from March to December 2012 with the LHC operating at a pp centre-of-mass energy of $\sqrt{s} = 8$ TeV. Candidate signal events are selected using a trigger based on an $E_{\mathrm{T}}^{\mathrm{miss}}$ selection, which is found to be 99% efficient for events passing the offline selection of $E_{\mathrm{T}}^{\mathrm{miss}} > 150$ GeV. The trigger efficiency variations over data-taking periods are

[1] ATLAS uses a right-handed coordinate system with its origin at the nominal interaction point (IP) in the centre of the detector and the z-axis along the beam pipe. The x-axis points from the IP to the centre of the LHC ring, and the y axis points upward. Cylindrical coordinates (r, ϕ) are used in the transverse plane, ϕ being the azimuthal angle around the beam pipe. The pseudorapidity is defined in terms of the polar angle θ as $\eta = -\ln\tan(\theta/2)$. The distance ΔR in the $\eta - \phi$ space is defined as $\Delta R = \sqrt{(\Delta\eta)^2 + (\Delta\phi)^2}$.

measured to be less than 1% after the offline requirements. After the application of beam, detector, and data-quality requirements, the total luminosity considered corresponds to 20.1 fb^{-1}. The uncertainty on the integrated luminosity is ±2.8%. It is derived, following the same methodology as that detailed in Ref. [35], from a preliminary calibration of the luminosity scale derived from beam-separation scans performed in November 2012. Events with electrons or muons in the final state are used to define control regions and are triggered by single- or di-lepton triggers with a total luminosity of 20.3 fb^{-1}. A $p_{\mathrm{T}} > 25$ GeV selection is applied to the highest p_{T} electron or muon to ensure the trigger selection is fully efficient.

3 Simulated event samples

Simulated Monte Carlo (MC) event samples are used to aid in the description of the background and to model the SUSY signal. All SM MC samples utilised in the analysis are produced using the ATLAS Underlying Event Tune 2B [36] and are processed through the ATLAS detector simulation [37] based on GEANT4 [38] or passed through a fast simulation using a parameterisation of the performance of the ATLAS electromagnetic and hadronic calorimeters [39]. The effect of multiple pp interactions per bunch crossing is also taken into account.

The $t\bar{t}$ background is simulated with Powheg [40] interfaced to Pythia6 [41] for the fragmentation and the hadronisation processes. The top-quark mass is fixed at 172.5 GeV, and the next-to-leading order (NLO) parton distribution function (PDF) set CT10 [42] is used. Alpgen [43] and Powheg samples interfaced with Herwig for the fragmentation and the hadronisation processes, including Jimmy [44] for the underlying event description, are used to estimate the generator and fragmentation systematic uncertainties, while AcerMC [45] interfaced to Pythia6 samples are used to estimate the hadronisation and showering uncertainties. Single top production for the s-channel and Wt processes is simulated with Mc@Nlo interfaced to Herwig+Jimmy, while the t-channel process is simulated with AcerMC interfaced to Pythia6 and using PDF set CTEQ6L1 [42]. Samples of $t\bar{t}$+W/Z are generated using the leading order generator MadGraph [46] interfaced to Pythia6 for the fragmentation and the hadronisation processes. Samples of Z/γ^* and samples of W production in association with up to five jets are produced with Sherpa. are MC samples of dibosons (ZZ, WZ and WW) decaying to final states with 2, 3 and 4 leptons are generated using Powheg+Pythia6.

The background predictions are normalised to theoretical cross sections, calculated including higher-order QCD corrections where available, and are compared to data in appropriate control regions. The inclusive cross section for Z+jets and W+jets is calculated with DYNNLO [47] with the MSTW 2008 next-to-next-to-leading order PDF set [48]. Approximate NLO+NNLL (next-to-next-to-leading-logarithm) cross sections are used in the normalisation of the $t\bar{t}$ [49] and Wt [50] samples. Cross sections calculated at NLO are used for the $t\bar{t} + W$ and $t\bar{t} + Z$ samples [51] and for the diboson samples [52].

The SUSY signal samples are generated using MadGraph interfaced to Pythia6 in order to ensure an accurate treatment of the initial-state radiation (ISR), using the PDF set CTEQ6L1. Additional samples where the ISR parameters are varied are generated to evaluate the ISR systematic uncertainty. Signal cross sections are calculated to next-to-leading order in the strong coupling constant, adding the resummation of soft gluon emission at next-to-leading-logarithmic accuracy (NLO+NLL) [53–55]. The nominal cross section and the uncertainty are taken from an envelope of cross section predictions using different PDF sets and factorisation and renormalisation scales, as described in Ref. [56].

4 Object reconstruction

Jets are reconstructed from three-dimensional calorimeter energy clusters using the anti-k_t jet algorithm [57, 58] with a radius parameter of 0.4. The measured jet energy is corrected for inhomogeneities

and for the non-compensating nature of the calorimeter by weighting energy deposits arising from electromagnetic and hadronic showers using correction factors derived from MC simulations and validated with data [59]. An additional calibration is subsequently applied to the corrected jet energies, relating the response of the calorimeter to the true jet energy. The impact of additional collisions in the same or neighbouring bunch crossings is accounted for using corrections derived as a function of the average number of interactions per event and of number of reconstructed primary vertices. Jets are required to have transverse momentum $p_{\mathrm{T}} > 20$ GeV, and are reconstructed in the range $|\eta| < 4.9$.

Events are rejected if they include jets failing the quality criteria described in Ref. [59]. To further reject spurious jet signals originating from cosmic rays or detector malfunctions, additional criteria are applied on the charged p_{T} fraction (chf), defined as the ratio between the sum of the p_{T} of all tracks associated to the jet and the jet p_{T}, and on the fraction of the jet energy contained in the electromagnetic layers of the calorimeter (emf). Events are rejected if any of the two leading jets with $p_T > 100$ GeV and $|\eta| < 2.0$ satisfies either $chf < 0.02$ or both $chf < 0.05$ and $emf > 0.9$. To remove jets from additional pp collisions, all jets with $p_{\mathrm{T}} < 50$ GeV and $|\eta| < 2.5$ are required to have at least one track identified as coming from the primary vertex.

Jets within the nominal acceptance of the ID ($|\eta| < 2.5$) and with $p_{\mathrm{T}} > 20$ GeV, are identified as originating from a b-quark (b-tagged) by using the impact parameter of the ID tracks, the secondary vertex reconstruction and the topology of b- and c-hadron decays inside the jet. The b-tagging algorithm [60] uses a multivariate technique and, for this analysis, is configured to achieve an efficiency of 60% for tagging b-jets in a MC sample of $t\bar{t}$ events with a corresponding rejection of 580, 8 and 23 against light quarks, c-quarks and τ leptons, respectively.

Electrons are reconstructed from energy clusters in the electromagnetic calorimeter matched to a track in the ID. Electron candidates are required to have $p_{\mathrm{T}} > 7$ GeV and $|\eta| < 2.47$ and must satisfy the "medium" selection criteria described in Ref. [61]. Electrons used for the control regions are selected using the "tight" criteria, $p_{\mathrm{T}} > 20$ GeV, and with an additional isolation requirement that the total momentum of charged tracks in a cone of $\Delta R < 0.2$ around the candidate be less than 10% of the reconstructed p_{T}. Muon candidates are identified using a match between an extrapolated ID track and one or more track segments in the muon spectrometer, and are required to have $p_{\mathrm{T}} > 6$ GeV and $|\eta| < 2.4$. Muons used in the control regions are also required to have $p_{\mathrm{T}} > 20$ GeV and less than 1.8 GeV deposited in the calorimeter in a cone of $\Delta R < 0.2$ around the candidate.

Any electron or muon candidate with a distance $\Delta R < 0.4$ to the closest jet is discarded.

The missing transverse momentum, $\mathbf{p}_{\mathrm{T}}^{\mathrm{miss}}$, and its magnitude, $E_{\mathrm{T}}^{\mathrm{miss}}$, is constructed as the vector sum of the transverse momentum of all p_{T} >10 GeV muons, p_{T} >10 GeV electrons, p_{T} >20 GeV jets, and calibrated calorimeter energy clusters with $|\eta|$ <4.9 not associated to these objects [62].

5 Event selection

Two sets of signal regions are defined to provide sensitivity to the kinematic topologies associated to different mass-splittings between the sbottom or the stop and the neutralino mass. In all cases, the presence of at least one primary vertex (with at least five associated tracks with $p_{\mathrm{T}} > 0.4$ GeV) is required. Events are selected with $E_{\mathrm{T}}^{\mathrm{miss}} > 150$ GeV, two b-jets and no electrons or muons identified in the final state. Jets within $|\eta| < 2.8$ are ordered according to their p_{T}, with n being their total number, and are used to define the following event level variables:

– $\Delta\phi_{\mathrm{min}}$: defined as the minimum azimuthal distance, $\Delta\phi$, between any of the leading three jets and the $\mathbf{p}_{\mathrm{T}}^{\mathrm{miss}}$.

$$\Delta\phi_{\mathrm{min}} = \min(|\phi_1 - \phi_{\mathbf{p}_{\mathrm{T}}^{\mathrm{miss}}}|, |\phi_2 - \phi_{\mathbf{p}_{\mathrm{T}}^{\mathrm{miss}}}|, |\phi_3 - \phi_{\mathbf{p}_{\mathrm{T}}^{\mathrm{miss}}}|). \quad (1)$$

Background multijet events are predominantly characterised by small values of $\Delta\phi_{\mathrm{min}}$.

– m_{eff}: defined as the scalar sum of the p_{T} of the n jets and the $E_{\text{T}}^{\text{miss}}$.

$$m_{\text{eff}} = \sum_{i=1}^{n} (p_{\text{T}}^{\text{jet}})_i + E_{\text{T}}^{\text{miss}}. \tag{2}$$

where the index refers to the p_{T}-ordered list of jets.

– $H_{\text{T},3}$ defined as the scalar sum of the p_{T} of the n jets, without including the three leading jets:

$$H_{\text{T},3} = \sum_{i=4}^{n} (p_{\text{T}}^{\text{jet}})_i. \tag{3}$$

where the index refers to the p_{T}-ordered list of jets.

– m_{bb}: defined as the invariant mass of the two b-tagged jets in the event.

– m_{CT}: the contransverse mass [63] is a kinematic variable that can be used to measure the masses of pair-produced semi-invisibly decaying heavy particles. For two identical decays of heavy particles into two visible particles (or particle aggregates) v_1 and v_2, and into invisible particles, m_{CT} is defined as:

$$m_{\text{CT}}^2(v_1, v_2) = [E_{\text{T}}(v_1) + E_{\text{T}}(v_2)]^2 - [\mathbf{p}_{\text{T}}(v_1) - \mathbf{p}_{\text{T}}(v_2)]^2 , \tag{4}$$

where $E_{\text{T}} = \sqrt{p_{\text{T}}^2 + m^2}$. In this analysis, v_1 and v_2 are the two b-jets from the squark decay and invisible particles the two $\tilde{\chi}_1^0$. The contransverse mass is an invariant under equal and opposite boosts of the parent particles in the transverse plane. For parent particles produced with small transverse boosts, m_{CT} is bounded from above by an analytical combination of particle masses. This bound is saturated when the two visible objects are co-linear. For $t\bar{t}$ events this kinematic bound is at 135 GeV. In the case of the sbottom pair production the bound is given by:

$$m_{\text{CT}}^{\text{max}} = \frac{m^2(\tilde{b}) - m^2(\tilde{\chi}_1^0)}{m(\tilde{b})}. \tag{5}$$

A similar equation can be written for the stop pair production in terms of $m_{\tilde{t}_1}$ and $m_{\tilde{\chi}_1^\pm}$. A correction to m_{CT} for transverse boost due to ISR is also applied [64].

The definition of the two signal regions is summarised in Table 1. Signal region A (SRA) targets signal events with large mass splitting between the squark and the neutralino, identifying two b-tagged leading jets as the sbottom or stop decay products. Events are rejected if any further central ($|\eta| < 2.8$) jets are found with $p_{\text{T}} > 50$ GeV. Multijet background is suppressed by selecting events with large $\Delta\phi_{\text{min}}$ and $E_{\text{T}}^{\text{miss}}/m_{\text{eff}}$. The requirement $m_{bb} > 200$ GeV is added to reduce the top and associated production of Z with heavy flavour jets backgrounds. As a final selection, five different thresholds on m_{CT} ranging from 150 GeV to 350 GeV are applied. For a signal point corresponding to $m_{\tilde{b}_1} = 500$ GeV and $m_{\tilde{\chi}_1^0} = 1$ GeV, 3% of the simulated events are retained by the SRA selection with $m_{\text{CT}} > 250$ GeV.

Signal region B (SRB) is defined to enhance the sensitivity in the region with a small squark-neutralino mass difference by explicitly selecting final state events with a high-p_{T} jet produced as initial state radiation recoiling against the squark pair system. High thresholds on the leading jet and on the missing transverse momentum, which are required to be almost back-to-back in ϕ, are imposed. The leading jet is required to be not b-tagged and two additional jets are required to be b-tagged. As for SRA, the multijet background is suppressed with appropriate selections on $\Delta\phi_{\text{min}}$ and $E_{\text{T}}^{\text{miss}}/m_{\text{eff}}$. A final upper requirement on the additional hadronic activity in the event, $H_{\text{T},3}$ <50 GeV completes the selection for SRB. For a signal point corresponding to $m_{\tilde{b}_1} = 300$ GeV and $m_{\tilde{\chi}_1^0} = 270$ GeV, 10% of the events are retained by the SRB selection.

Description	Signal Regions	
	SRA	SRB
Trigger	$E_{\mathrm{T}}^{\mathrm{miss}} > 150$ GeV	
Event cleaning	Common to all SR	
Lepton veto	No e/μ after overlap removal with $p_{\mathrm{T}} > 7(6)$ GeV for $e(\mu)$.	
$E_{\mathrm{T}}^{\mathrm{miss}}$	> 150 GeV	> 250 GeV
Leading jet $p_{\mathrm{T}}(j_1)$	> 130 GeV, $\lvert\eta\rvert < 2.8$	> 150 GeV, $\lvert\eta\rvert < 2.8$
Second jet $p_{\mathrm{T}}(j_2)$	> 50 GeV, $\lvert\eta\rvert < 2.8$	> 40 GeV, $\lvert\eta\rvert < 2.8$
Third jet $p_{\mathrm{T}}(j_3)$	veto if > 50 GeV, $\lvert\eta\rvert < 2.8$	> 40 GeV, $\lvert\eta\rvert < 2.8$
$\Delta\phi(\mathbf{p}_{\mathrm{T}}^{\mathrm{miss}}, j_1)$	-	> 2.5
b-jet multiplicity	leading 2 jets ($p_{\mathrm{T}} > 50$ GeV, $\lvert\eta\rvert < 2.5$)	2nd- and 3rd-leading jets ($p_{\mathrm{T}} > 40$GeV, $\lvert\eta\rvert < 2.5$)
	$n_{b\text{-jets}} = 2$	
$\Delta\phi_{\mathrm{min}}$	> 0.4	> 0.4
$E_{\mathrm{T}}^{\mathrm{miss}}/m_{\mathrm{eff}}(j_1, j_2, (j_3))$	> 0.25 (2 jets)	> 0.25 (3 jets)
m_{CT}	$> 150, 200, 250, 300, 350$ GeV	-
$H_{\mathrm{T},3}$	-	< 50 GeV
m_{bb}	> 200 GeV	-

Table 1: Summary of the event selection in each signal region.

6 Background estimate

The dominant SM background processes in the signal regions are the production of W or Z boson in association with heavy flavour jets (referred to as W+hf and Z+hf) and the production of top quarks. Z+hf followed by $Z \to \nu\bar{\nu}$ has the same signature as the signal being searched for and it is the dominant background in SRA. Top (dominant in SRB) and W+hf production satisfy the signal region seletions when a charged lepton is produced but the event is not rejected, either because the lepton is a hadronically decaying τ, or because the electron or muon is not reconstructed. The dominant backgrounds are normalised in dedicated control regions (CRs) and then extrapolated to the signal regions using MC simulated data. The control regions, detailed below, are defined by explicitly requiring the presence of leptons (electrons or muons) in the final state together with further selections similar to those of the corresponding signal regions. The single top contribution accounts for 5% to 20% of the total top background contribution, depending on the signal region considered, and is added to the $t\bar{t}$ background contribution with a relative normalisation corresponding to that predicted by the MC, as described in Section 3.

The background from multijet production is estimated from data using a procedure described in detail in Ref. [65], which consists of smearing the jet response of low-$E_{\mathrm{T}}^{\mathrm{miss}}$ seed events. The Gaussian core of the jet response function is obtained from di-jet events, while the non-Gaussian tails are obtained from three-jet events, where the $E_{\mathrm{T}}^{\mathrm{miss}}$ can be unambiguously associated to the mis-measurement of one of the jets. The contribution from multijet production in the control regions is found to be negligible.

Finally, contributions from diboson and $t\bar{t}+W/Z$ processes are sub-dominant and they are collectively called "Others" in the following. They are estimated from MC for both the signal and the control regions.

For SRA, the contributions from top, Z+jets and W+jets production are estimated simultaneously with a likelihood fit to three control regions. For SRB it is difficult to identify a control region that probes the W+jets background normalisation. Therefore, this contribution is estimated purely from MC as described in Section 3 and only control regions for top and Z+jets are defined.

A set of same-flavour opposite-sign 2-lepton control regions with dilepton invariant mass around the Z mass ($75 < \mathrm{m}_{\ell\ell} < 105$ GeV) provides a data sample dominated by Z production. For these control regions, labelled in the following as CRA_SF and CRB_SF, the p_{T} of the leptons is added vectorially to the $\mathbf{p}_{\mathrm{T}}^{\mathrm{miss}}$ to mimic the expected missing transverse momentum spectrum of $Z \to \nu\bar{\nu}$ events. In addition, the p_{T} of the leading lepton is required to be above 90 GeV in order to further enhance the Z production contribution. In the case of CRA_SF, a $m_{bb} > 200$ GeV selection is also imposed.

The set of control regions with exactly one lepton (e, μ) in the final state provides a data sample dominated by top and W+jets production. A selection on the tranverse mass (m_{T}) is applied, 40 GeV $< \mathrm{m}_{\mathrm{T}} < 100$ GeV, where m_{T} is defined as:

$$\mathrm{m}_{\mathrm{T}} = \sqrt{2p_{\mathrm{T}}^{\mathrm{lep}} E_{\mathrm{T}}^{\mathrm{miss}} - 2\mathbf{p}_{\mathrm{T}}^{\mathrm{lep}} \cdot \mathbf{p}_{\mathrm{T}}^{\mathrm{miss}}} \tag{6}$$

In the following, these control regions are labelled as CRA_1L and CRB_1L. CRA_1L is used to estimate the contribution of the W+jets background, which is enhanced by the selection $m_{\mathrm{CT}} > 150$ GeV in SRA. CRB_1L is used to estimate the top background in SRB.

To estimate the top production in SRA, a different-flavour opposite-sign 2-lepton control region (CRA_DF) is defined requiring one electron and one muon in the final state with $m_{e\mu} > 50$ GeV and $m_{\mathrm{CT}} > 75$ GeV.

The definitions of each of the control regions are summarised in Tables 2 and 3.

The distribution of the m_{CT} variable in CRA_1L (before the m_{CT} selection) and of the leading lepton p_{T} in CRA_SF are shown before the fit in Figure 1. Similarly, the transverse mass distribution between the leading lepton and the $E_{\mathrm{T}}^{\mathrm{miss}}$ in CRB_1L (before the m_{T} selection) and the invariant mass distribution of the two leptons in CRB_SF (before the $\mathrm{m}_{\ell\ell}$ selection) are shown in Figure 2. In these figures the

CRA_1L	CRA_SF	CRA_DF
1 tight electron or muon	$e^{\pm}e^{\mp}$ or $\mu^{\pm}\mu^{\mp}$	$e^{\pm}\mu^{\mp}$
Veto additional baseline leptons. $p_{\mathrm{T}}(e)$ >7 GeV $p_{\mathrm{T}}(\mu)$ >6 GeV		
two reconstructed jets (veto on 3rd jet) ($p_{\mathrm{T}} > 50$)		
$p_{\mathrm{T}}(j_1) > 130$ GeV $p_{\mathrm{T}}(j_2) > 50$ GeV $E_{\mathrm{T}}^{\mathrm{miss}} > 100$ GeV	$p_{\mathrm{T}}(j_1) > 50$ GeV $p_{\mathrm{T}}(j_2) > 50$ GeV $E_{\mathrm{T}}^{\mathrm{miss}}$(lepton-corrected) > 100 GeV	$p_{\mathrm{T}}(j_1) > 130$ GeV $p_{\mathrm{T}}(j_2) > 50$ GeV $E_{\mathrm{T}}^{\mathrm{miss}} > 100$ GeV
two reconstructed b-jets ($p_{\mathrm{T}} > 50$)		
40 GeV < $\mathrm{m_T}$ < 100 GeV	75 GeV < $\mathrm{m}_{\ell\ell}$ < 105 GeV	$\mathrm{m}_{\ell\ell}$ > 50 GeV
$m_{\mathrm{CT}} > 150$ GeV	lepton $p_{\mathrm{T}} > 90$ GeV	$m_{\mathrm{CT}} > 75$ GeV
–	$m_{bb} > 200$ GeV	–

Table 2: Definition of the three SRA control regions.

CRB_1L	CRB_SF
1 tight electron or muon	$e^{\pm}e^{\mp}$ or $\mu^{\pm}\mu^{\mp}$
Veto additional baseline leptons. $p_{\mathrm{T}}(e)$ >7 GeV $p_{\mathrm{T}}(\mu)$ >6 GeV	
three reconstructed jets ($p_{\mathrm{T}} > 40$)	
$p_{\mathrm{T}}(j_1) > 130$ GeV $E_{\mathrm{T}}^{\mathrm{miss}} > 120$ GeV	$p_{\mathrm{T}}(j_1) > 50$ GeV $E_{\mathrm{T}}^{\mathrm{miss}}$(lepton-corrected) > 100 GeV
j_1 anti b-tagged; j_2 and j_3 b-tagged	
40 GeV < $\mathrm{m_T}$ < 100 GeV	75 GeV < $\mathrm{m}_{\ell\ell}$ < 105 GeV
–	lepton $p_{\mathrm{T}} > 90$ GeV
$H_{\mathrm{T},3} < 50$ GeV	

Table 3: Definition of the two SRB control regions.

data set used corresponds to an integrated luminosity of 20.3 fb^{-1} and the normalisations as described in Section 3 are assumed.

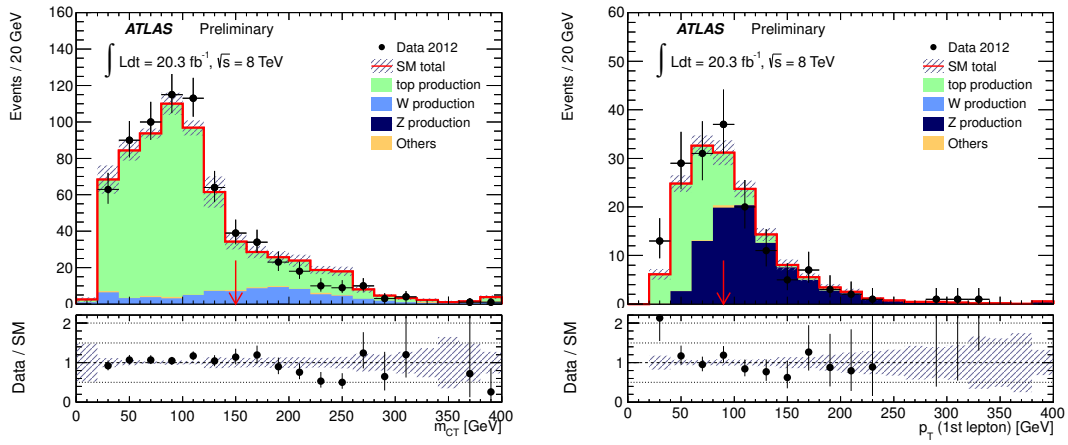

Figure 1: Left: m_{CT} distribution in CRA_1L omitting the requirement on the m_{CT} variable. Right: leading lepton p_{T} distribution in CRA_SF with all the selections applied omitting the requirement on this variable. The red arrow indicates where a selection on the corresponding variable is applied. The shaded band includes both detector and theoretical systematic uncertainties. The SM prediction is normalised according to the MC expectations.

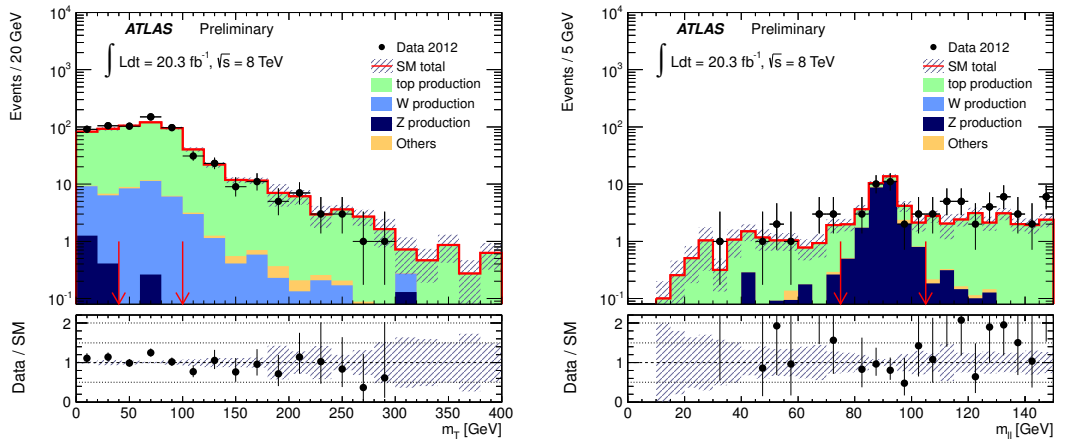

Figure 2: Left: transverse mass distribution between the lepton and the $E_{\mathrm{T}}^{\mathrm{miss}}$ in CRB_1L omitting the $\mathrm{m_T}$ requirement. Right: dilepton invariant mass distribution in CRB_SF omitting the $\mathrm{m}_{\ell\ell}$ requirement. The red arrow indicates where a selection on the corresponding variable is applied. The shaded band includes both detector and theoretical systematic uncertainties. The SM prediction is normalised according to the MC expectations.

The observed numbers of events in the different CRs are used to generate internally consistent SM background estimates for each of the SRs via a likelihood fit. This procedure enables CR correlations due to common systematic uncertainties and contamination by other SM processes and/or SUSY signal events, when a particular model is considered for exclusion. Systematic uncertainties, discussed in detail in Section 7, are treated as nuisance parameters in the fit and are constrained with Gaussian functions taking into account correlations between sample estimates. The likelihood function is built as the product of Poisson probability functions, describing the observed and expected number of events in the control

Channel	**CRA_1L**	**CRA_SF**	**CRA_DF**
Observed events	136	68	76
Fitted background events			
Total SM	136 ± 12	68 ± 8	76 ± 9
Top production	92 ± 17	10.2 ± 1.4	75 ± 9
Z production	0.42 ± 0.12	57 ± 8	$0.07^{+0.11}_{-0.07}$
W production	40 ± 20	< 0.1	0.07 ± 0.03
Others	3.8 ± 2.0	0.44 ± 0.19	0.39 ± 0.14
MC expected events			
Top production	100	11.0	82
Z production	0.46	63	0.08
W production	48	< 0.1	0.08
Others	3.8	0.44	0.39

Table 4: Results of the fit for the control regions adopted for SRA. Yields as derived from MC using theoretical cross sections are also shown. Uncertainties quoted include statistical and detector-related systematic effects. The central values of the fitted sum of backgrounds in the control regions agree with the observations by construction. The uncertainty on the total background estimate can be smaller than some of the individual uncertainties due to anticorrelations.

and (when excluding SUSY models) signal regions, and the constraints on the nuisance parameters. As a result, the impact of some of the systematic uncertainties that are correlated between the CRs and the corresponding SR is reduced.

The free parameters of the fit are the top, W+jets and Z+jets overall normalisation values for SRA, and the top and Z+jets normalisation values for SRB. The contributions from all other background processes are fixed at the value expected from MC. The fit results in the control regions are summarised in Tables 4 and 5 for SRA and SRB, respectively. These results are found to be compatible with MC predictions before the fit, also given in the tables.

The reliability of the MC extrapolation of the SM background estimation outside of the control regions is evaluated in several validation regions. The first set of validation regions is defined with the same kinematic selection as the control regions but requiring only one jet to be b-tagged. They are used to verify the performance of the b-tagging algorithm in an increased statistics sample. A second set of validation regions is defined with an identical selection to the signal regions, but inverting one of the requirements. In all cases these validation regions are background dominated with a potential signal contamination of less than 20% in the signal models considered. For SRA, two validation regions are explored by imposing either $m_{\mathrm{CT}} < 100$ GeV or $m_{bb} < 200$ GeV. To validate SRB, a validation region with the selection $H_{\mathrm{T},3} > 50$ GeV is defined as well as a second validation region with two leptons of different flavour to verify the normalisation of the top background. Good agreement is found with less than one standard deviation between the expectations and the number of observed events in all cases.

7 Systematic uncertainties

The dominant detector-related systematic effects are due to the uncertainties on the jet energy scale (JES) and resolution (JER) and on the b-tagging efficiency. The impact of these uncertainties is reduced through the normalisation of the dominant backgrounds in the control regions with kinematic selections resembling those of the corresponding signal region.

Channel	**CRB_1L**	**CRB_SF**
Observed events	350	29
Fitted background events		
Total SM	350 ± 19	29 ± 5
Top production	323 ± 24	11.2 ± 1.4
Z production	0.25 ± 0.12	17 ± 6
W production	26 ± 16	< 0.1
Others	1.1 ± 0.5	0.72 ± 0.27
MC expected events		
Top production	293	10.2
Z production	0.38	25
W production	25	< 0.1
Others	1.1	0.72

Table 5: Results of the fit for the control regions adopted for SRB. Yields as derived from MC using theoretical cross sections are also shown. Uncertainties quoted include statistical and detector-related systematic effects. The central values of the fitted sum of backgrounds in the control regions agree with the observations by construction. The uncertainty on the total background estimate can be smaller than some of the individual uncertainties due to anticorrelations. The W estimation is normalised using the nominal theoretical cross section and with the associated uncertainties discussed in Section 7.

The JES uncertainty has been determined using the techniques described in Refs. [66, 67], leading to a slight dependence upon p_{T}, η, jet flavour, number of primary vertices and proximity to adjacent jets. The JER uncertainty is obtained from in-situ measurements of the jet response asymmetry in di-jet events [68]. These uncertainties on jets are propagated to the $E_{\mathrm{T}}^{\mathrm{miss}}$ measurement, and additional uncertainties on $E_{\mathrm{T}}^{\mathrm{miss}}$ arising from energy deposits not associated with any reconstructed objects are also included. The relative impact on the event yields from the JES (JER) uncertainty is between 1–4% (1–8%) in the different SRA regions and of 7% (8%) in SRB.

The b-tagging uncertainty is evaluated by varying p_{T} and flavour dependent scale factors applied to each jet in the simulation within a range that reflects the systematic uncertainty on the measured tagging efficiency and rejection rates. The relative impact of this uncertainty in the final event yield is dominated by the uncertainty on the b-tagging efficiency. The uncertainty amounts to 2–9% in the different SRA regions and 2% in SRB.

In the case of SRB, an uncertainty is also associated to the requirement that jets with $p_{\mathrm{T}} < 50$ GeV have at least one track originating from the primary vertex. It has a relative impact on the final event yields of 6%.

Theoretical uncertainties in the modelling of the $t\bar{t}$+jets background are assessed. The uncertainty due to the choice of the MC generator is estimated by comparing Powheg to Alpgen generators, both interfaced to the Herwig+Jimmy parton shower (PS) calculations. The PS uncertainty is estimated by comparing samples generated with Powheg interfaced to either Pythia6 or Herwig+Jimmy. The uncertainty due to the ambiguity in the renormalisation and factorisation scales is estimated by independently changing them by a factor of two up and down. The uncertainty in the ISR and final state radiation (FSR) is estimated by comparing AcerMC samples generated with different amounts of ISF/FSR. The PDF uncertainties are derived by varying the 52 PDFs in the CT10 NLO error set following the Hessian method and rescaling to 68% confidence level. Since $t\bar{t}$ and single top production are treated together, these theoretical uncertainties are also assigned to the single top contribution and it has been checked that they account for the difference in event kinematics between the samples. The final relative uncertainties

Channel	SRA, m_{CT} selection					SRB
	150 GeV	200 GeV	250 GeV	300 GeV	350 GeV	
Observed	103	48	14	7	3	58
Total SM	92 ± 12	38 ± 6	15.3 ± 2.7	5.8 ± 1.2	2.6 ± 0.6	50 ± 9
Top production	11.3 ± 1.8	2.5 ± 1.4	0.45 ± 0.25	< 0.01	< 0.01	34 ± 7
Z production	64 ± 10	28 ± 5	11.1 ± 2.1	4.7 ± 0.9	2.0 ± 0.4	8 ± 3
W production	12 ± 6	4.6 ± 2.5	2.0 ± 1.1	1.0 ± 0.5	0.48 ± 0.27	5 ± 4
Others	4.3 ± 1.5	3.3 ± 1.3	1.8 ± 0.6	0.12 ± 0.11	$0.10^{+0.12}_{-0.10}$	1.5 ± 0.7
Multijet production	0.21 ± 0.21	0.06 ± 0.06	0.02 ± 0.02	< 0.01	< 0.01	0.2 ± 0.2

Table 6: For each signal region, the observed event yield is compared with the background prediction obtained from the fit. Uncertainties include statistical and detector and theoretical systematic uncertainties.

on the yields due to theoretical uncertainties in top production modeling are less than 0.7% in SRA and 4% in SRB, mostly dominated by PS and scale uncertainties.

Uncertainties on the W/Z+jets simulation are evaluated by comparing the Sherpa and Alpgen generators and by varying the Sherpa scales related to the matching scheme, the strong coupling constant, and the renormalisation and the factorisation scales. The PDF uncertainties are evaluated following the same procedure as for the top background. For SRB, the W production is estimated from MC and an additional uncertainty of 26% due to the W+hf contribution is included [69]. The relative uncertainties on the yields are in the range 0.3–3.1% in SRA, mostly dominated by the difference between Sherpa and Alpgen. For SRB a 5% uncertainty is assigned to Z+hf and 9% to W+hf, the latter uncertainty being dominated by the MC normalisation.

An uncertainty of 100% is derived for the multijet prediction from studying a variation of the resolution function. Finally uncertainties of 30% and of 50% for the cross section of $t\bar{t} + W$ and of $t\bar{t} + Z$ production, respectively, are assigned [51, 70].

8 Results and interpretation

The number of data events observed in each signal region is reported in Table 6, together with the SM background expectation after the fit. Figures 3 and 4 show the comparison between the SM prediction and the observed data for some relevant kinematic distributions in SRA and SRB, respectively. An example of a SUSY process with a large mass difference between the squark and the lightest neutralino is also shown for reference in each case.

No significant excess above the SM expectations is observed in any of the signal regions. The results are used to derive upper limits on the number of expected beyond SM (BSM) events for each signal region, and on the corresponding cross section, σ_{vis}, defined as

$$\sigma_{\text{vis}} = \sigma \cdot A \cdot \epsilon \tag{7}$$

where σ, A and ϵ are, respectively, the production cross section, the acceptance and the selection efficiency for a generic BSM signal. The 95% confidence level (CL) limits are computed using the *CLs* prescription [71]. Table 7 summarises, for each signal region, the estimated SM background yield, the observed number of events, and the expected and observed upper limit on event yields from a BSM signal and on σ_{vis}.

Results are interpreted in different SUSY scenarios assuming a SUSY particle mass hierarchy such that the lightest third generation squark decays exclusively via $\tilde{b}_1 \to b\tilde{\chi}_1^0$, in case of sbottom, and $\tilde{t}_1 \to b\tilde{\chi}_1^{\pm}$, in case of stop pair production. For the latter case, two different Δm values between the lightest chargino and neutralino are probed to assess the impact of the lepton and jet vetoes applied in the analysis.

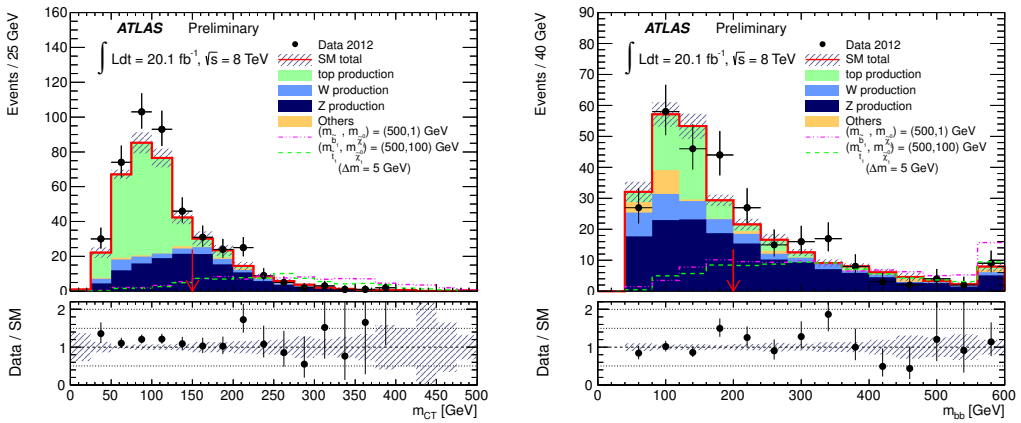

Figure 3: Left: m_{CT} distribution in SRA with all the selections cuts applied except the m_{CT} thresholds. Right: m_{bb} distribution in SRA with all selection cuts applied including $m_{\mathrm{CT}} > 150$ GeV. The shaded band includes statistical and both detector and theoretical systematic uncertainties. The backgrounds are normalised to the values determined in the fit. The red arrow indicates where a selection on the corresponding variable is applied. For illustration the distributions expected for two signal models are displayed. The models correspond to $m_{\tilde{b}_1} = 500$ GeV and $m_{\tilde{\chi}_1^0} = 1$ GeV (purple dash-dot line) and $m_{\tilde{t}_1} = 500$ GeV and $m_{\tilde{\chi}_1^0} = 100$ GeV. The rightmost bin in the figures includes the overflows.

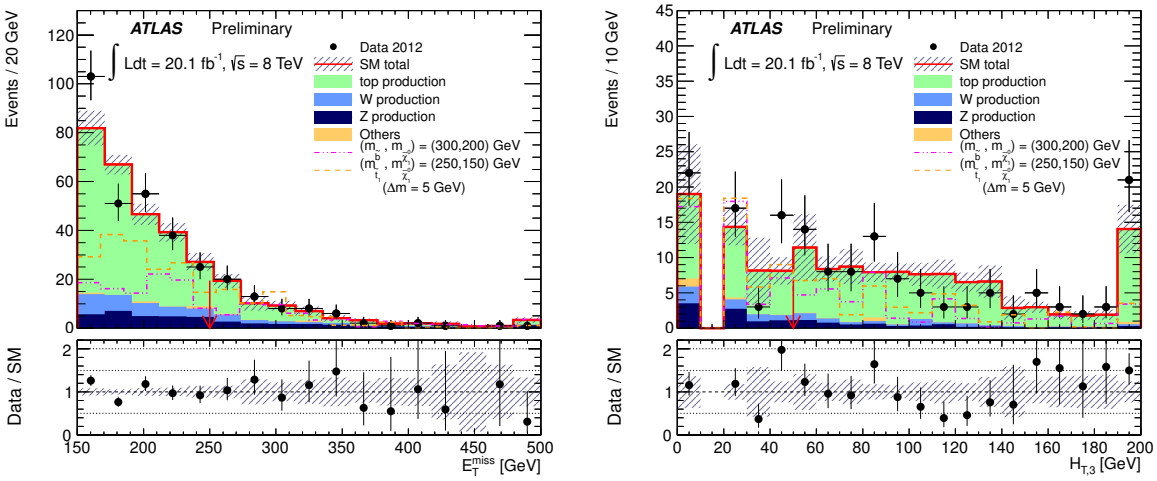

Figure 4: Left: $E_{\mathrm{T}}^{\mathrm{miss}}$ distribution after all SRB selections applied except the final $E_{\mathrm{T}}^{\mathrm{miss}}$ requirement. Right: distribution of $H_{\mathrm{T},3}$ after all SRB selections are applied except the $H_{\mathrm{T},3}$ requirement. Since jets have $p_{\mathrm{T}} > 20$ GeV by construction, the bin on the left contains events where no additional jets are present ($H_{\mathrm{T},3}$ =0 GeV) while the second bin is empty. The shaded band includes statistical and both detector and theoretical systematic uncertainties. The backgrounds are normalised to the values determined in the fit. The red arrow indicates where a selection on the corresponding variable is applied. For illustration the distributions expected for two signal models are displayed. The models correspond to $m_{\tilde{b}_1} = 300$ GeV and $m_{\tilde{\chi}_1^0} = 200$ GeV (purple dash-dot line) and $m_{\tilde{t}_1} = 250$ GeV and $m_{\tilde{\chi}_1^0} = 150$ GeV. The rightmost bin in the figures includes the overflows.

Signal Regions	Bkg. estimate	Obs. data	95% CL upper limit			
			on BSM event yield		on σ_{vis} (fb)	
			expected	observed	expected	observed
SRA ($m_{\text{CT}} > 150$ GeV)	92 ± 12	103	31^{+12}_{-8}	39.2	$1.5^{+0.6}_{-0.4}$	1.95
SRA ($m_{\text{CT}} > 200$ GeV)	38 ± 6	48	18^{+7}_{-5}	25.9	$0.89^{+0.35}_{-0.25}$	1.29
SRA ($m_{\text{CT}} > 250$ GeV)	15.3 ± 2.7	14	$10.0^{+4.6}_{-2.9}$	9.2	$0.50^{+0.23}_{-0.14}$	0.46
SRA ($m_{\text{CT}} > 300$ GeV)	5.8 ± 1.2	7	$6.5^{+3.3}_{-2.1}$	7.6	$0.32^{+0.16}_{-0.1}$	0.38
SRA ($m_{\text{CT}} > 350$ GeV)	2.6 ± 0.6	3	$4.7^{+2.6}_{-1.6}$	5.2	$0.23^{+0.13}_{-0.08}$	0.26
SRB	50 ± 9	58	24^{+9}_{-7}	30.0	$1.21^{+0.45}_{-0.35}$	1.49

Table 7: Expected and observed event yields with the corresponding upper limits on generic BSM signal yields and $\sigma_{\text{vis}} = \sigma \cdot A \cdot \epsilon$ for all the signal regions defined.

Systematic uncertainties on the signal acceptance include experimental uncertainties, mostly dominated by b-tagging (20 – 30% in SRA, ∼ 15 – 30% in SRB) and JES (4 – 30% in SRA, 20 – 40% in SRB) uncertainties. These uncertainties are assumed to be fully correlated with those of the background.

For SRB, the uncertainties due to the modelling of the ISR processes are assessed by changing the strength of the parton shower controlled by Pythia6 and by changing by a factor of 2 and 1/2 the following three parameters: (i) the factorisation and renormalisation scales after k_{T}-clustering of the event; (ii) the matching distance between a parton and a jet; (iii) the scale at which α_S is evaluated at every parton radiation step. The relative changes due to each of these individual variations are assumed to be uncorrelated and are added in quadrature. The overall uncertainty due to ISR depends on the mass difference between the squark and the LSP, with a maximum value of 30% on the signal acceptance when the mass difference is of the order of 10 GeV and fast dropping down to a plateau of 7–10% at a 25 GeV of mass difference. This uncertainty has a negligible dependence on the squark mass for the mass range considered in this analysis.

Figure 5 shows the observed (solid lines) and expected (dashed lines) exclusion limits obtained by taking, for each signal mass configuration, the signal region with the best expected limit. These limits are obtained using a likelihood test which compares the observed event rates in the signal regions with the fitted background expectation and the eventual signal contamination in the corresponding CRs for a given model. Sensitivity to scenarios with large mass difference (> 100 GeV) between the $\tilde{b}_1$ and the $\tilde{\chi}^0_1$ is achieved with the successive m_{CT} thresholds used in SRA. Sensitivity to more compressed scenarios is predominantly achieved with the dedicated SRB selection.

For the sbottom pair production decaying only into $b\tilde{\chi}^0_1$, sbottom masses up to 620 GeV are excluded at 95% CL for $m_{\tilde{\chi}^0_1} < 150$ GeV. Differences in mass above 70 GeV between the $\tilde{b}_1$ and the $\tilde{\chi}^0_1$ are excluded up to sbottom masses of 250 GeV. If the branching ratio of $\tilde{b}_1 \to b\tilde{\chi}^0_1$ is reduced to 60% and assuming that the analysis is not sensitive to other possible decays, the excluded upper limit on the sbottom mass for $m_{\tilde{\chi}^0_1} < 150$ GeV is reduced to 480 GeV. Similarly for $m_{\tilde{b}_1} = 250$ GeV, the upper limit on $m_{\tilde{\chi}^0_1}$ is reduced by 30 GeV.

For stop pair production decaying only into $b\tilde{\chi}^\pm_1$, stop masses up to 580 GeV (440 GeV) are excluded for $\Delta m = m_{\tilde{\chi}^\pm_1} - m_{\tilde{\chi}^0_1}$ =5 GeV (20 GeV) and for $m_{\tilde{\chi}^0_1} = 100$ GeV. For $\Delta m = 5$ GeV (20 GeV), neutralino masses up to 250 GeV (220 GeV) are excluded for $m_{\tilde{t}_1} = 450$ GeV.

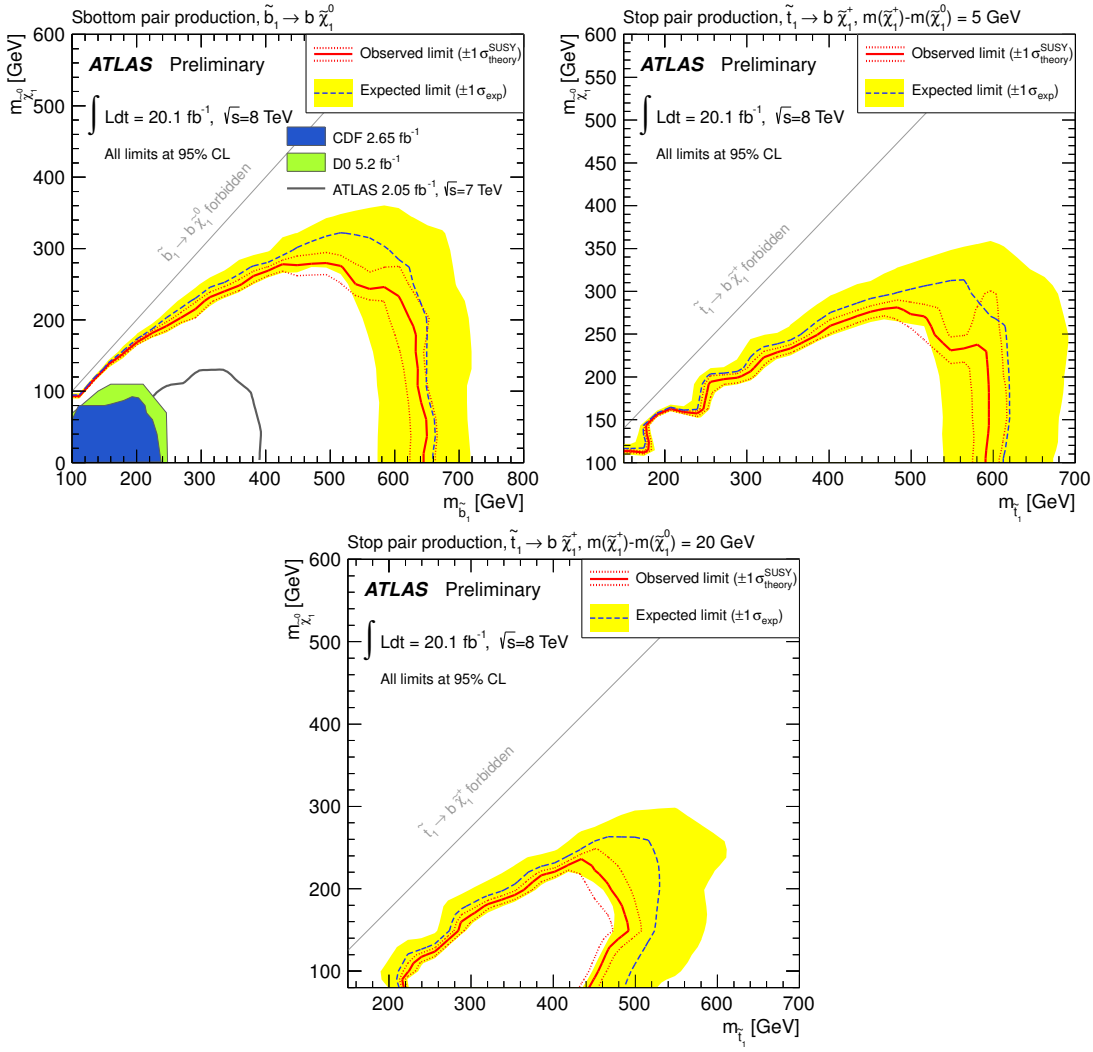

Figure 5: Expected and observed exclusion limits at 95% CL for the different MSSM scenarios considered. Left: $(m_{\tilde{b}_1}, m_{\tilde{\chi}_1^0})$ mass plane. Right: $(m_{\tilde{t}_1}, m_{\tilde{\chi}_1^0})$ mass plane with $m_{\tilde{\chi}_1^\pm} - m_{\tilde{\chi}_1^0} = 5$ GeV. Bottom: $(m_{\tilde{t}_1}, m_{\tilde{\chi}_1^0})$ mass plane with $m_{\tilde{\chi}_1^\pm} - m_{\tilde{\chi}_1^0} = 20$ GeV. The signal region providing the best expected CLs exclusion limit is chosen at every point. The dashed (solid) lines show the expected (observed) limits, including all uncertainties except for the theoretical signal cross section uncertainty (PDF and scale). The bands around the expected limits show the $\pm1\sigma$ results. The dotted lines around the observed limits represent the results obtained when moving the nominal signal cross section up or down by the $\pm1\sigma$ theoretical uncertainty. Previous limits published by ATLAS [22], CDF [31] and D0 [32] are also shown. In the case of the direct stop, only points in the parameter space not excluded by the LEP lower limit on the lightest chargino mass of 103.5 GeV [33] are considered.

9 Conclusions

The results of a search for third generation squark pair production in pp collisions at $\sqrt{s} = 8$ TeV, based on 20.1 fb^{-1} of ATLAS data are reported. Events with large $E_{\mathrm{T}}^{\mathrm{miss}}$ and two b-tagged jets are analysed. The results are in agreement with SM predictions for backgrounds and translate into 95% C.L. upper limits on the sbottom (stop) and neutralino masses in a given MSSM scenario for which the exclusive decay $\tilde{b}_1 \to b\tilde{\chi}_1^0$ ($\tilde{t}_1 \to b\tilde{\chi}_1^{\pm}$) is assumed. For the sbottom pair production decaying only into $b\tilde{\chi}_1^0$, sbottom masses up to 620 GeV are excluded at 95% CL for $m_{\tilde{\chi}_1^0} < 150$ GeV. Differences in mass above 70 GeV between the $\tilde{b}_1$ and the $\tilde{\chi}_1^0$ are excluded up to sbottom masses of 250 GeV. These limits significantly extend previous results.

For stop pair production decaying only into $b\tilde{\chi}_1^{\pm}$, stop masses up to 580 GeV (440 GeV) are excluded for $\Delta m = m_{\tilde{\chi}_1^{\pm}} - m_{\tilde{\chi}_1^0}$ =5 GeV (20 GeV) and for $m_{\tilde{\chi}_1^0} = 100$ GeV. For $\Delta m = 5$ GeV (20 GeV), neutralino masses up to 250 GeV (220 GeV) are excluded for $m_{\tilde{t}_1} = 450$ GeV.

References

[1] H. Miyazawa, *Baryon Number Changing Currents*, Prog. Theor. Phys. **36 (6)** (1966) 1266–1276.

[2] P. Ramond, *Dual Theory for Free Fermions*, Phys. Rev. **D3** (1971) 2415–2418.

[3] Y. A. Gol'fand and E. P. Likhtman, *Extension of the Algebra of Poincare Group Generators and Violation of p Invariance*, JETP Lett. **13** (1971) 323–326. [Pisma Zh.Eksp.Teor.Fiz.13:452-455,1971].

[4] A. Neveu and J. H. Schwarz, *Factorizable dual model of pions*, Nucl. Phys. **B31** (1971) 86–112.

[5] A. Neveu and J. H. Schwarz, *Quark Model of Dual Pions*, Phys. Rev. **D4** (1971) 1109–1111.

[6] J. Gervais and B. Sakita, *Field theory interpretation of supergauges in dual models*, Nucl. Phys. **B34** (1971) 632–639.

[7] D. V. Volkov and V. P. Akulov, *Is the Neutrino a Goldstone Particle?*, Phys. Lett. **B46** (1973) 109–110.

[8] J. Wess and B. Zumino, *A Lagrangian Model Invariant Under Supergauge Transformations*, Phys. Lett. **B49** (1974) 52.

[9] J. Wess and B. Zumino, *Supergauge Transformations in Four-Dimensions*, Nucl. Phys. **B70** (1974) 39–50.

[10] S. Weinberg, *Implications of Dynamical Symmetry Breaking*, Phys. Rev. **D13** (1976) 974–996.

[11] E. Gildener, *Gauge Symmetry Hierarchies*, Phys. Rev. **D14** (1976) 1667.

[12] S. Weinberg, *Implications of Dynamical Symmetry Breaking: An Addendum*, Phys. Rev. **D19** (1979) 1277–1280.

[13] L. Susskind, *Dynamics of Spontaneous Symmetry Breaking in the Weinberg- Salam Theory*, Phys. Rev. **D20** (1979) 2619–2625.

[14] P. Fayet, *Supersymmetry and Weak, Electromagnetic and Strong Interactions*, Phys. Lett. **B64** (1976) 159.

[15] P. Fayet, *Spontaneously Broken Supersymmetric Theories of Weak, Electromagnetic and Strong Interactions*, Phys. Lett. **B69** (1977) 489.

[16] G. R. Farrar and P. Fayet, *Phenomenology of the Production, Decay, and Detection of New Hadronic States Associated with Supersymmetry*, Phys. Lett. **B76** (1978) 575–579.

[17] P. Fayet, *Relations Between the Masses of the Superpartners of Leptons and Quarks, the Goldstino Couplings and the Neutral Currents*, Phys. Lett. **B84** (1979) 416.

[18] S. Dimopoulos and H. Georgi, *Softly Broken Supersymmetry and SU(5)*, Nucl. Phys. **B193** (1981) 150.

[19] L. Evans and P. Bryant, *LHC Machine*, JINST **3** (2008) S08001.

[20] R. Barbieri and G. Giudice, *Upper Bounds on Supersymmetric Particle Masses*, Nucl. Phys. **B306** (1988) 63.

[21] B. de Carlos and J. Casas, *One loop analysis of the electroweak breaking in supersymmetric models and the fine tuning problem*, Phys. Lett. **B309** (1993) 320–328, arXiv:hep-ph/9303291 [hep-ph].

[22] ATLAS Collaboration, *Search for Scalar Bottom Quark Pair Production with the ATLAS Detector in pp Collisions at* $\sqrt{s} = 7$ *TeV*, Phys. Rev. Lett. **108** (2012) 181802, arXiv:1112.3832 [hep-ex].

[23] ATLAS Collaboration, *Search for a heavy top-quark partner in final states with two leptons with the ATLAS detector at the LHC*, JHEP **1211** (2012) 094, arXiv:1209.4186 [hep-ex].

[24] ATLAS Collaboration, *Search for light top squark pair production in final states with leptons and b-jets with the ATLAS detector in* $\sqrt{s} = 7$ *TeV proton-proton collisions*, Phys. Lett. **B720** (2013) 13–31, arXiv:1209.2102 [hep-ex].

[25] ATLAS Collaboration, *Search for light scalar top quark pair production in final states with two leptons with the ATLAS detector in* $\sqrt{s} = 7$ *TeV proton-proton collisions*, Eur. Phys. J **C72** (2012) 2237, arXiv:1208.4305 [hep-ex].

[26] ATLAS Collaboration, *Search for direct top squark pair production in final states with one isolated lepton, jets, and missing transverse momentum in* $\sqrt{s} = 7$ *TeV pp collisions using 4.7* fb^{-1} *of ATLAS data*, Phys. Rev. Lett. **109** (2012) 211803, arXiv:1208.2590 [hep-ex].

[27] ATLAS Collaboration, *Search for a supersymmetric partner to the top quark in final states with jets and missing transverse momentum at* $\sqrt{s} = 7$ *TeV with the ATLAS detector*, Phys. Rev. Lett. **109** (2012) 211802, arXiv:1208.1447 [hep-ex].

[28] CMS Collaboration, *Search for new physics in events with same-sign dileptons and b jets in pp collisions at* $\sqrt{s} = 8$ *TeV*, JHEP **1303** (2013) 037, arXiv:1212.6194 [hep-ex].

[29] CMS Collaboration, *Search for supersymmetry in final states with missing transverse energy and 0, 1, 2, or at least 3 b-quark jets in 7 TeV pp collisions using the variable* α_T, JHEP **1301** (2013) 077, arXiv:1210.8115 [hep-ex].

[30] CMS Collaboration, *Search for supersymmetry in hadronic final states with missing transverse energy using the variables* α_T *and b-quark multiplicity in pp collisions at* $\sqrt{s} = 8$ *TeV*, arXiv:1303.2985 [hep-ex].

[31] CDF Collaboration, T. Aaltonen et al., *Search for the Production of Scalar Bottom Quarks in* $p\bar{p}$ *collisions at* $\sqrt{s} = 1.96$ *TeV*, Phys. Rev. Lett. **105** (2010) 081802, arXiv:1005.3600 [hep-ex].

[32] D0 Collaboration, V.M. Abazov et al., *Search for scalar bottom quarks and third-generation leptoquarks in* pp^- *bar collisions at* $\sqrt{s} = 1.96$ *TeV*, Phys. Lett. **B693** (2010) 95–101, arXiv:1005.2222 [hep-ex].

[33] LEP SUSY Working Group (ALEPH, DELPHI, L3, OPAL), Notes LEPSUSYWG/01-03.1 and 04-01.1, http://lepsusy.web.cern.ch/lepsusy/Welcome.html.

[34] ATLAS Collaboration, *The ATLAS Experiment at the CERN Large Hadron Collider*, JINST **3** (2008) S08003.

[35] ATLAS Collaboration, *Improved luminosity determination in pp collisions at* $\sqrt{s} = 7$ *TeV using the ATLAS detector at the LHC*, arXiv:1302.4393 [hep-ex].

[36] ATLAS Collaboration, *ATLAS tunes of PYTHIA 6 and Pythia 8 for MC11*, ATL-PHYS-PUB-2011-009 (2010). http://cds.cern.ch/record/1363300.

[37] ATLAS Collaboration, *The ATLAS Simulation Infrastructure*, Eur. Phys. J **C70** (2010) 823–874, arXiv:1005.4568 [physics.ins-det].

[38] GEANT4 Collaboration, Agostinelli et al., *GEANT4: A simulation toolkit*, Nucl. Instrum. Meth. **A506** (2003) 250–303.

[39] ATLAS Collaboration, *The simulation principle and performance of the ATLAS fast calorimeter simulation FastCaloSim*, ATL-PHYS-PUB-2010-013 (2010). http://cds.cern.ch/record/1300517.

[40] S. Frixione, P. Nason, and C. Oleari, *Matching NLO QCD computations with Parton Shower simulations: the POWHEG method*, JHEP **0711** (2007) 070, arXiv:0709.2092 [hep-ph].

[41] T. Sjostrand, S. Mrenna, and P. Skands, *PYTHIA 6.4 physics and manual*, JHEP **0605** (2006) 026, arXiv:hep-ph/0603175.

[42] P. M. Nadolsky, H.-L. Lai, Q.-H. Cao, J. Huston, J. Pumplin, et al., *Implications of CTEQ global analysis for collider observables*, Phys. Rev. **D78** (2008) 013004, arXiv:0802.0007 [hep-ph].

[43] M. Mangano et al., *ALPGEN, a generator for hard multiparton processes in hadronic collisions*, JHEP **0307** (2003) 001, arXiv:hep-ph/0206293.

[44] J. Butterworth, J. R. Forshaw, and M. Seymour, *Multiparton interactions in photoproduction at HERA*, Z. Phys. **C72** (1996) 637–646, arXiv:hep-ph/9601371 [hep-ph].

[45] B. P. Kersevan and E. Richter-Was, *The Monte Carlo event generator AcerMC version 2.0 with interfaces to PYTHIA 6.2 and HERWIG 6.5*, arXiv:hep-ph/0405247 [hep-ph].

[46] J. Alwall, M. Herquet, F. Maltoni, O. Mattelaer, and T. Stelzer, *MadGraph 5 : Going Beyond*, JHEP **1106** (2011) 128, arXiv:1106.0522 [hep-ph].

[47] S. Catani, L. Cieri, G. Ferrera, D. de Florian, and M. Grazzini, *Vector boson production at hadron colliders: A Fully exclusive QCD calculation at NNLO*, Phys. Rev. Lett. **103** (2009) 082001, arXiv:0903.2120 [hep-ph].

[48] A. Martin et al., *Parton distributions for the LHC*, Eur. Phys. J. C **63** (2009) 189–285.

[49] M. Aliev, H. Lacker, U. Langenfeld, S. Moch, P. Uwer, et al., *HATHOR: HAdronic Top and Heavy quarks crOss section calculatoR*, Comput. Phys. Commun. **182** (2011) 1034–1046, arXiv:1007.1327 [hep-ph].

[50] N. Kidonakis, *Two-loop soft anomalous dimensions for single top quark associated production with a W^- or H^-*, Phys. Rev. **D82** (2010) 054018, arXiv:1005.4451 [hep-ph].

[51] M. Garzelli, A. Kardos, C. Papadopoulos, and Z. Trocsanyi, *$t\bar{t}$ W and $t\bar{t}$ Z Hadroproduction at NLO accuracy in QCD with Parton Shower and Hadronization effects*, arXiv:1208.2665 [hep-ph].

[52] T. Binoth, M. Ciccolini, N. Kauer, and M. Kramer, *Gluon-induced W-boson pair production at the LHC*, JHEP **0612** (2006) 046, arXiv:hep-ph/0611170 [hep-ph].

[53] W. Beenakker, M. Kramer, T. Plehn, M. Spira, and P. Zerwas, *Stop production at hadron colliders*, Nucl. Phys. **B515** (1998) 3–14, arXiv:hep-ph/9710451 [hep-ph].

[54] W. Beenakker, S. Brensing, M. Kramer, A. Kulesza, E. Laenen, et al., *Supersymmetric top and bottom squark production at hadron colliders*, JHEP **1008** (2010) 098, arXiv:1006.4771 [hep-ph].

[55] W. Beenakker, S. Brensing, M. Kramer, A. Kulesza, E. Laenen, et al., *Squark and Gluino Hadroproduction*, Int. Jour. Mod. Phys. **A26** (2011) 2637–2664, arXiv:1105.1110 [hep-ph].

[56] M. Kramer et al., *Supersymmetry production cross sections in pp collisions at* $\sqrt{s}$ *= 7 TeV*, arXiv:1206.2892 [hep-ph] (2012), arXiv:1206.2892 [hep-ph].

[57] M. Cacciari, G. P. Salam, and G. Soyez, *The anti-*k_t *jet clustering algorithm*, JHEP **0804** (2008) 063, arXiv:0802.1189 [hep-ph].

[58] M. Cacciari and G. P. Salam, *Dispelling the* N^3 *myth for the* k_t *jet-finder*, Phys. Lett. **B641** (2006) 57–61, arXiv:hep-ph/0512210 [hep-ph].

[59] ATLAS Collaboration, *Jet energy scale and its systematic uncertainty in proton-proton collisions at* $\sqrt{s}$*=7 TeV in ATLAS 2010 data*, ATLAS-CONF-2011-032 (2011). https://cdsweb.cern.ch/record/1337782.

[60] ATLAS Collaboration, *Commissioning of the ATLAS high-performance b-tagging algorithms in the 7 TeV collision data*, ATLAS-CONF-2011-102 (2011). https://cdsweb.cern.ch/record/1369219.

[61] ATLAS Collaboration, *Electron performance measurements with the ATLAS detector using the 2010 LHC proton-proton collision data*, Eur. Phys. J **C72** (2012) 1909, arXiv:1110.3174 [hep-ex].

[62] ATLAS Collaboration, *Performance of Missing Transverse Momentum Reconstruction in Proton-Proton Collisions at 7 TeV with ATLAS*, Eur. Phys. J **C72** (2012) 1844, arXiv:1108.5602 [hep-ex].

[63] D. Tovey, *On measuring the masses of pair-produced semi-invisibly decaying particles at hadron colliders*, JHEP **0804** (2008) 034, arXiv:0802.2879 [hep-ph].

[64] G. Polesello and D. Tovey, *Supersymmetric particle mass measurement with the boost- corrected contransverse mass*, JHEP **1003** (2010) 030, arXiv:0910.0174 [hep-ph].

[65] ATLAS Collaboration, *Search for squarks and gluinos with the ATLAS detector in final states with jets and missing transverse momentum using 4.7* fb^{-1} *of* $\sqrt{s}$ *= 7 TeV proton-proton collision data*, Phys. Rev. **D87** (2013) 012008, arXiv:1208.0949 [hep-ex].

[66] ATLAS Collaboration, *Jet energy measurement with the ATLAS detector in proton-proton collisions at* $\sqrt{s}$ *= 7 TeV*, Eur. Phys. J **C73** (2013) 2304, arXiv:1112.6426 [hep-ex].

[67] ATLAS Collaboration, *Single hadron response measurement and calorimeter jet energy scale uncertainty with the ATLAS detector at the LHC*, Eur. Phys. J **C73** (2013) 2305, arXiv:1203.1302 [hep-ex].

[68] ATLAS Collaboration, *Jet energy resolution and selection efficiency relative to track jets from in-situ techniques with the ATLAS Detector Using Proton-Proton Collisions at a Center of Mass Energy* $\sqrt{s}$ *= 7 TeV*, ATLAS-CONF-2010-054 (2010). http://cdsweb.cern.ch/record/1281311.

[69] ATLAS Collaboration, *Measurement of the cross-section for W boson production in association with b-jets in pp collisions at sqrt(s) = 7 TeV with the ATLAS detector*, arXiv:1302.2929 [hep-ex]. Submitted to JHEP.

[70] J. M. Campbell and R. K. Ellis, *$t\bar{t}W^{+-}$ production and decay at NLO*, JHEP **1207** (2012) 052, arXiv:1204.5678 [hep-ph].

[71] G. Cowan, K. Cranmer, E. Gross, and O. Vitells, *Power-Constrained Limits*, arXiv:1105.3166 [physics.data-an].

Appendix : auxiliary material

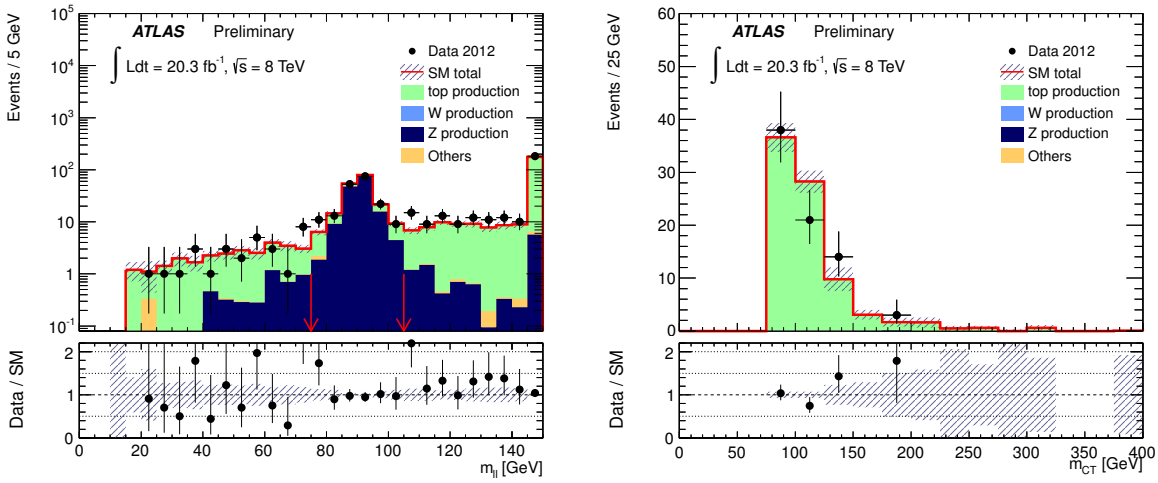

Figure 6: Left: di-lepton invariant mass distribution in CRA_SF omitting the $m_{\ell\ell}$ and m_{bb} cuts. Right: m_{CT} distribution in CRA_DF with all selections applied including $m_{\mathrm{CT}} > 75$ GeV. The shaded band includes both detector and theoretical systematic uncertainties. The SM prediction is normalised according to the MC expectations. The red arrow indicates where a selection on the corresponding variable is applied.

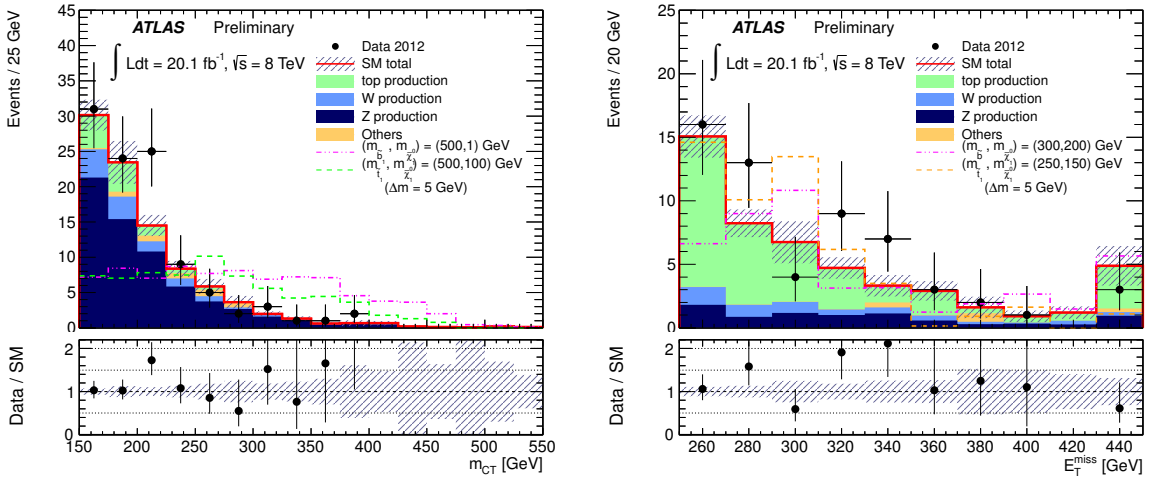

Figure 7: Left: m_{CT} distribution after the complete SRA is applied for the $m_{\mathrm{CT}} > 150$ GeV threshold. Right: $E_{\mathrm{T}}^{\mathrm{miss}}$ distribution after the complete SRB selection is applied. The shaded band includes statistical and both detector and theoretical systematic uncertainties. The backgrounds are normalised to the values determined in the fit. For illustration, the distributions expected for two relevant signal models in each of the regions are shown.

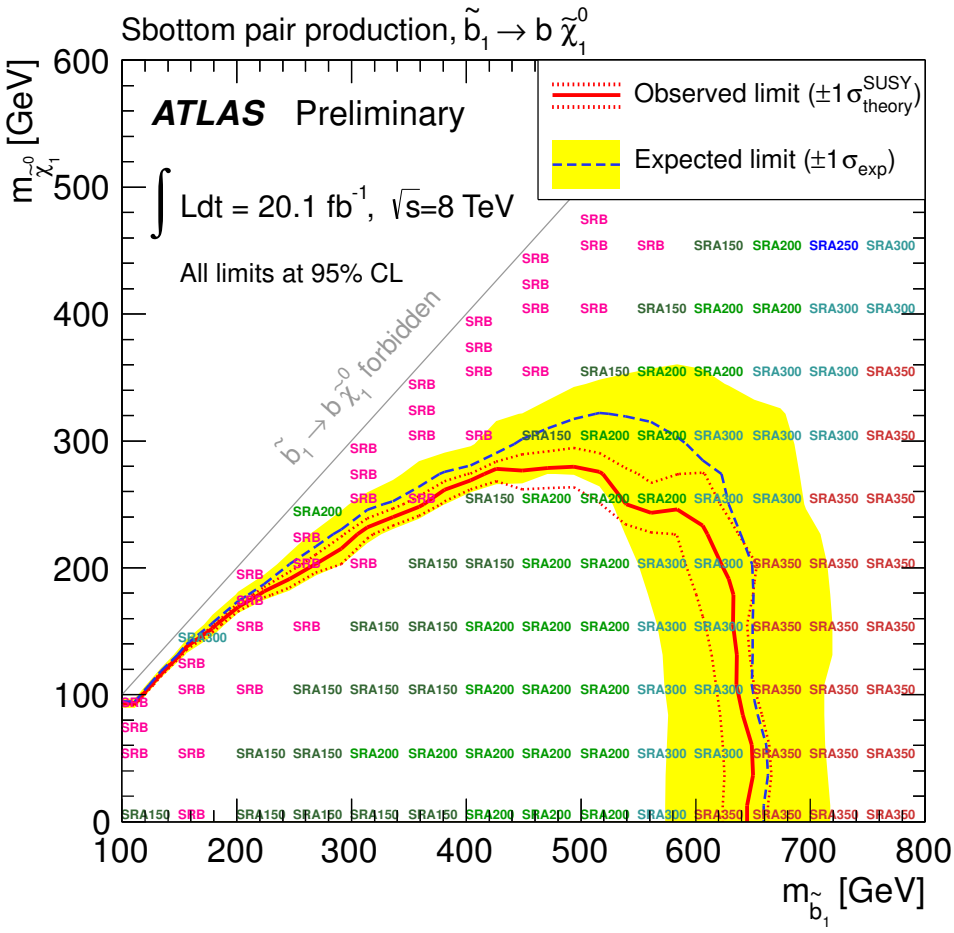

Figure 8: Expected and observed exclusion limits at 95% CL for the ($m_{\tilde{b}_1}$, $m_{\tilde{\chi}_1^0}$) mass plane. The dashed (solid) lines show the expected (observed) limits, including all uncertainties except for the theoretical signal cross section uncertainty (PDF and scale). The bands around the expected limits show the $\pm1\sigma$ results. The lines around the observed limits represent the results obtained when moving the nominal signal cross section up or down by the $\pm1\sigma$ theoretical uncertainty. The text shows the signal region providing the best expected sensitivity for the corresponding part of the figure. In the case of SRA, the number shown represents the m_{CT} threshold used.

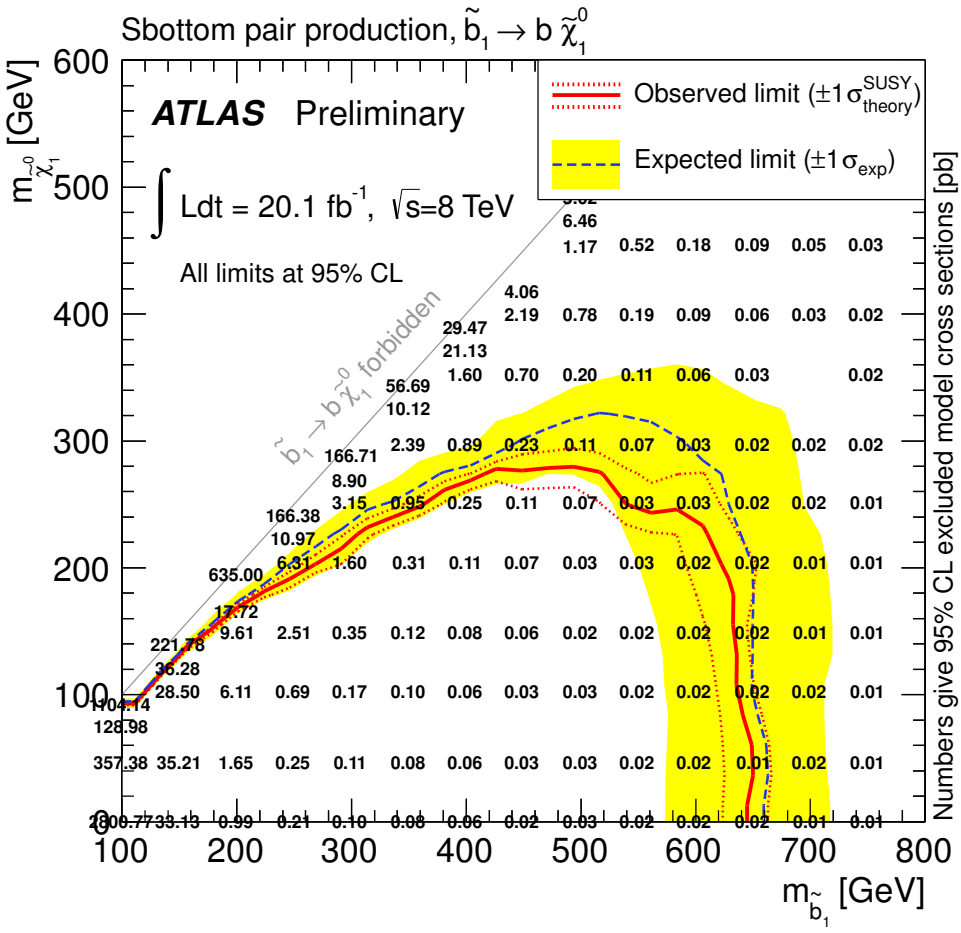

Figure 9: Expected and observed exclusion limits at 95% CL for the $(m_{\tilde{b}_1}, m_{\tilde{\chi}_1^0})$ mass plane. The dashed (solid) lines show the expected (observed) limits, including all uncertainties except for the theoretical signal cross section uncertainty (PDF and scale). The bands around the expected limits show the $\pm 1\sigma$ results. The lines around the observed limits represent the results obtained when moving the nominal signal cross section up or down by the $\pm 1\sigma$ theoretical uncertainty. Numbers represent the nominal observed excluded cross sections at 95% CL, once corrected by the luminosity and the efficiency times acceptance of the model itself.

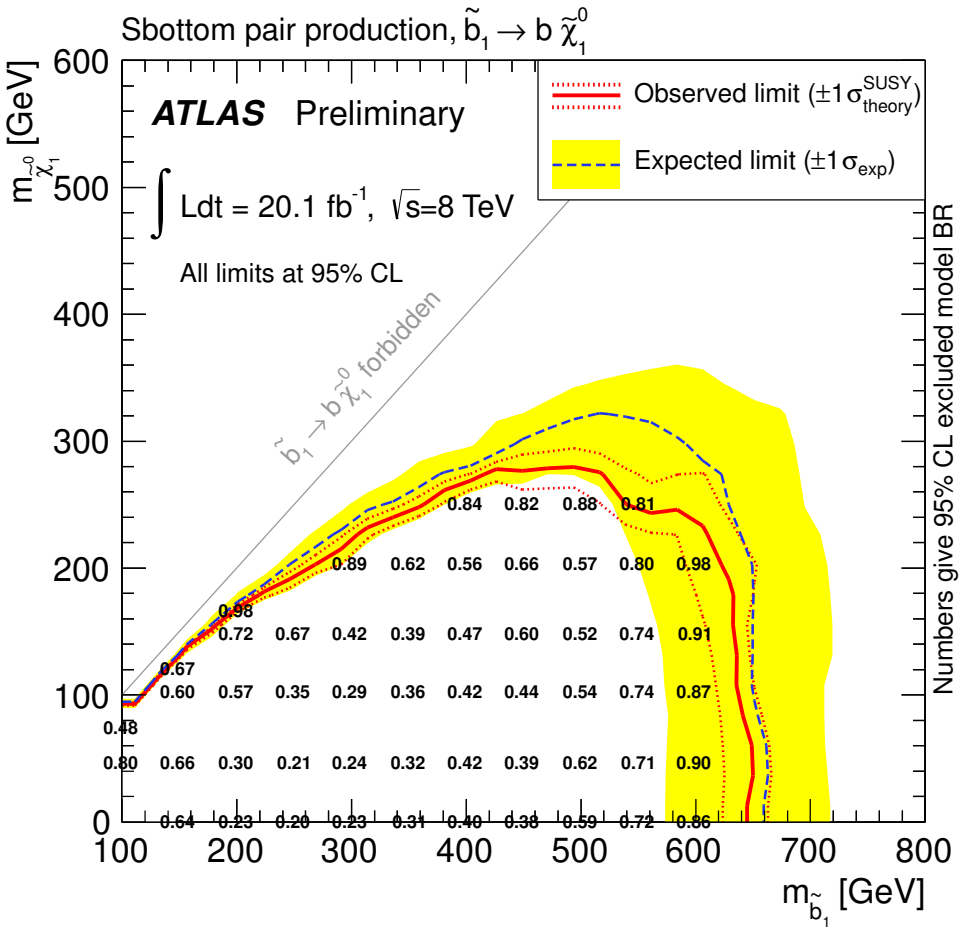

Figure 10: Impact of reducing the branching ratios of the sbottom decay into $b\chi_1^{\pm}$, assuming no sensitivity to the other decay possibilities. The numbers represent the maximum branching ratio excluded at 95% CL, taking the nominal cross section as reference.

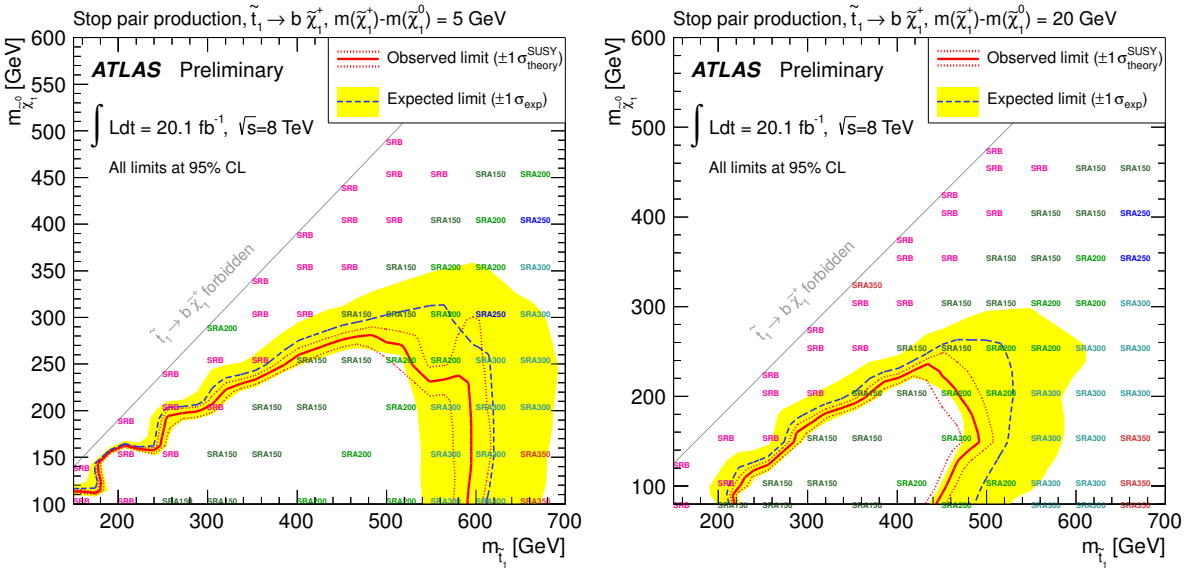

Figure 11: Expected and observed exclusion limits at 95% CL for the $(m_{\tilde{t}_1}, m_{\tilde{\chi}_1^0})$ mass plane with $\Delta m(\tilde{\chi}_1^\pm, \tilde{\chi}_1^0) = 5$ GeV (left) and 20 GeV (right). The dashed (solid) lines show the expected (observed) limits, including all uncertainties except for the theoretical signal cross section uncertainty (PDF and scale). The bands around the expected limits show the $\pm 1\sigma$ results. The lines around the observed limits represent the results obtained when moving the nominal signal cross section up or down by the $\pm 1\sigma$ theoretical uncertainty. Only models that are not excluded by the LEP lower limit on the lightest chargino mass of 103.5 GeV [33] are considered. The text shows the signal region providing the best expected sensitivity for the corresponding part of the figure. In the case of SRA, the number shown represents the m_{CT} threshold used.

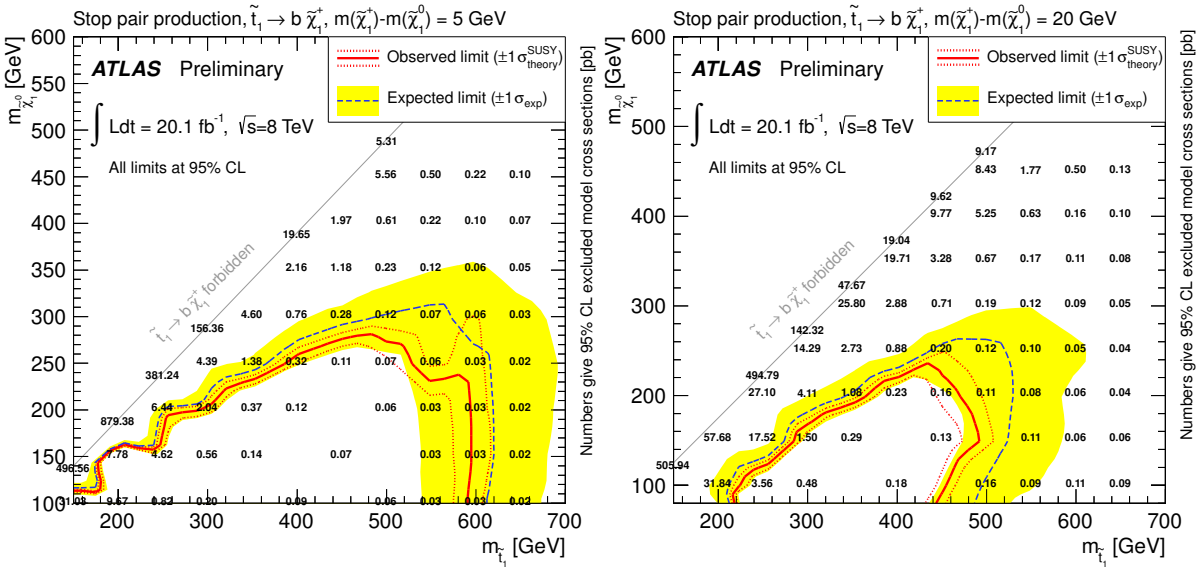

Figure 12: Expected and observed exclusion limits at 95% CL for the $(m_{\tilde{t}_1}, m_{\tilde{\chi}_1^0})$ mass plane with $\Delta m(\tilde{\chi}_1^\pm, \tilde{\chi}_1^0) = 5$ GeV (left) and 20 GeV (right). The dashed (solid) lines show the expected (observed) limits, including all uncertainties except for the theoretical signal cross section uncertainty (PDF and scale). The bands around the expected limits show the $\pm 1\sigma$ results. The lines around the observed limits represent the results obtained when moving the nominal signal cross section up or down by the $\pm 1\sigma$ theoretical uncertainty. Only models that are not excluded by the LEP lower limit on the lightest chargino mass of 103.5 GeV [33] are considered. Numbers represent the nominal observed excluded cross sections at 95% CL, once corrected by the luminosity and the efficiency times acceptance of the model itself.